



RESEARCH ARTICLE

10.1002/2015JC010891

Source regions and reflection of infragravity waves offshore of the U.S.s Pacific Northwest

Jennifer Neale¹, Nicholas Harmon¹, and Meric Srokosz²¹Ocean and Earth Science, National Oceanography Centre Southampton, University of Southampton, Southampton, UK,²National Oceanography Centre, University of Southampton Waterfront Campus, Southampton, UK

Key Points:

- Deep water infragravity wave directionality is obtained using cross correlation
- Reflection of infragravity waves at the coast is estimated
- Reflection at the North American Pacific coastline appears to be strong

Supporting Information:

- Supporting Information S1

Correspondence to:

J. Neale,
Jennifer.Neale@noc.soton.ac.uk

Citation:

Neale, J., N. Harmon, and M. Srokosz (2015), Source regions and reflection of infragravity waves offshore of the U.S.s Pacific Northwest, *J. Geophys. Res. Oceans*, 120, 6474–6491, doi:10.1002/2015JC010891.

Received 2 APR 2015

Accepted 8 SEP 2015

Accepted article online 11 SEP 2015

Published online 26 SEP 2015

Abstract Infragravity waves are oceanic surface gravity waves but with wavelengths (tens of km) and periods (>30 s) much longer than wind waves and swell. Mostly studied in shallow water, knowledge of infragravity waves in deep water has remained limited. Recent interest in deep water infragravity waves has been motivated by the error they may contribute to future high-resolution satellite radar altimetry measurements of sea level. Here deep water infragravity waves offshore of the Pacific Northwest of the U.S. were studied using differential pressure gauges which were deployed as part of the Cascadia Initiative array from September 2012 to May 2013. Cross correlation of the records revealed direction of infragravity wave propagation across the array, from which source regions were inferred. The dominant source was found to be the coastline to the east, associated with large wind waves and swell incident on the eastern side of the basin. The source shifted southward during northern-hemisphere summer, and on several days in the record infragravity waves arrived from the western side of the Pacific. Asymmetry of cross-correlation functions for five of these westerly arrivals was used to calculate the ratio of seaward to shoreward propagating energy, and hence estimate the strength of infragravity wave reflection at periods of 100–200 s. Reflection of these remote arrivals from the west appeared to be strong, with a lower bound estimate of $r = 0.49 \pm 0.29$ (reflection coefficient \pm standard error) and an upper bound estimate of $r = 0.74 \pm 0.06$. These results suggest that reflection at ocean boundaries may be an important consideration for infragravity waves in the deep ocean.

1. Introduction

Low-frequency infragravity waves are associated with wave groups of the higher-frequency sea waves and swell in the coastal zone. Two mechanisms have been proposed for the generation of infragravity waves from the short-wave groups. One is that the interaction of shoreward propagating swell creates “bound” or “forced” infragravity waves [Longuet-Higgins and Stewart, 1962; Herbers *et al.*, 1995a]. As the swell waves break, the forced infragravity waves are released as free infragravity waves and are reflected from the beach. Free infragravity waves satisfy the dispersion relation for surface gravity waves and have longer wavelengths than forced waves of the same frequency [Webb *et al.*, 1991]. The second mechanism is that infragravity waves are generated by a time-varying breakpoint, with standing waves shoreward of the breakpoint and progressive infragravity waves radiating seaward [Symonds *et al.*, 1982].

In either case, the seaward propagating free infragravity waves can have two fates: those that travel seaward at oblique angles can become refractively trapped along the shoreline as “edge waves” by a sloping beach or shelf [Herbers *et al.*, 1995a; Munk *et al.*, 1964]; those that propagate directly seaward can escape into the open ocean as “leaky waves” [Munk *et al.*, 1964]. Due to their long wavelength [Aucan and Ardhuin, 2013], only a small fraction of the infragravity energy escapes from the coast into the open ocean (<1%) [Webb *et al.*, 1991], with most being trapped within a few hundred meters of the shore. The amount of energy leaked into the open ocean for a given short-wave spectrum and coastline is poorly understood [Aucan and Ardhuin, 2013]. Variation in alongshore topography may be partly responsible [Uchiyama and McWilliams, 2008], although the model of Ardhuin *et al.* [2014] produces a good prediction of measured infragravity wave levels assuming a locally straight coast.

Infragravity waves that make it into the open ocean propagate with very little attenuation [Godin *et al.*, 2013], and it is possible to observe infragravity waves that have been generated from coasts thousands of kilometers away on the other side of an ocean basin [Herbers *et al.*, 1995a; Harmon *et al.*, 2012].

© 2015. The Authors.

This is an open access article under the terms of the Creative Commons Attribution License, which permits use, distribution and reproduction in any medium, provided the original work is properly cited.

Most studies of infragravity waves have been undertaken in shallow water on continental shelves where they are most energetic [Webb *et al.*, 1991] and instrumentation is more accessible. Here they are also known as “surf beat” or “swash,” and they are important for sediment transport and nearshore morphology [Aagaard and Greenwood, 2008; Reniers, 2004] and harbor oscillations [Okhiro and Guza, 1996]. The first studies were undertaken by Munk [1949] and Tucker [1950].

Infragravity waves in the deep ocean have received less attention than shallow water infragravity waves partly due to their very small amplitudes in the deep ocean (<1 cm) [Webb *et al.*, 1991], several cm at most [Aucan and Ardhuin, 2013]. However, there has recently been a resumed interest in infragravity waves in the deep ocean as they have been recognized as important for coupling processes in the ocean, ice, atmosphere, and solid earth [Godin *et al.*, 2013]. Aucan and Ardhuin [2013] have shown that infragravity waves in the deep ocean may add significant error to sea level measurements associated with submesoscale currents, which are due to be collected by future satellite radar altimetry missions. Bromirski *et al.* [2010] have recently shown that infragravity waves generated along the Pacific coast propagate transoceanic distances and can be implicated in the flexure and subsequent breakup of Antarctic ice shelves. Infragravity waves at frequencies below 0.004 Hz may transfer energy from the ocean to the atmosphere [Livneh *et al.*, 2007; Godin *et al.*, 2015]. The deformation of the seafloor under the pressure of infragravity waves is used in measurements of seafloor compliance to determine the shear velocity structure of the shallow oceanic crust [Crawford *et al.*, 1998], and the propagation of infragravity waves over a sloping seabed are thought to create low-frequency seismic noise known as Earth’s seismic hum [Rhie and Romanowicz, 2006; Ardhuin *et al.*, 2015].

Pressure sensors (or seismometers) deployed on the seafloor have been the most widely used approach to observe infragravity waves in the deep ocean [Godin *et al.*, 2013]. Using an array of pressure gauges in the southwestern Pacific off the South Island of New Zealand, Godin *et al.* [2014] observed strong directionality of the infragravity wavefield with the northwest coast of the South Island acting as a net source of infragravity wave energy. Webb *et al.* [1991] studied deep water infragravity waves in the Pacific during November 1988 and identified infragravity waves originating from the Gulf of Alaska, the northwest Pacific and the southern tip of South America, but little from the southern ocean or tropical western Pacific.

A further and more comprehensive study of infragravity waves in the deep ocean was undertaken by Aucan and Ardhuin [2013]. They analyzed pressure records from 40 locations in the Pacific and Atlantic oceans to determine spatial and temporal variability of infragravity wave energy at depths of 3–6 km. Their inferred infragravity significant wave heights were found to reach larger values than estimated in previous work, reaching over 4 cm in episodic events. Energy levels in the Atlantic and Pacific were found to be similar, and mid to high latitudes in both oceans displayed strong seasonal cycles associated with seasonal variability of wind waves.

Other studies have noted the arrival of infragravity waves which seem to have been generated right across the other side of the ocean basin [Harmon *et al.*, 2012], and a combined observational and modeling study [Rawat *et al.*, 2014] has shown the coherent propagation of large infragravity wave bursts from one side of the basin to the other. The latter study made use of a global numerical model of free infragravity wave generation and propagation that has been under development recently [Ardhuin *et al.*, 2014].

The aim of this study was to determine how strongly free infragravity waves reflect when they reach the coastline or shelf of an ocean basin. As far as the authors are aware, no estimate of deep water infragravity reflection has yet been made, although reflection from the shoreline has previously been estimated from pressure gauges in shallow waters <13 m in depth [e.g., Herbers *et al.*, 1995a; Sheremet, 2002] and from laboratory data [Battjes, 2004]. Studies such as these have found that infragravity waves reflect strongly from the shore with reflection coefficients above 0.6. Considering that infragravity waves are capable of propagating right across the oceans, reflection at the ocean boundary, whether at the shoreline or shelf, may be important for infragravity energy in the deep ocean. Here we present estimates of the directionality and reflection coefficient for the infragravity wavefield offshore of the Pacific Northwest of the U.S.

2. Data and Methods

To measure deep water infragravity waves, we used differential Pressure Gauge (DPG) records from the Cascadia Initiative array [Toomey *et al.*, 2014] between September 2012 and May 2013, downloaded from the

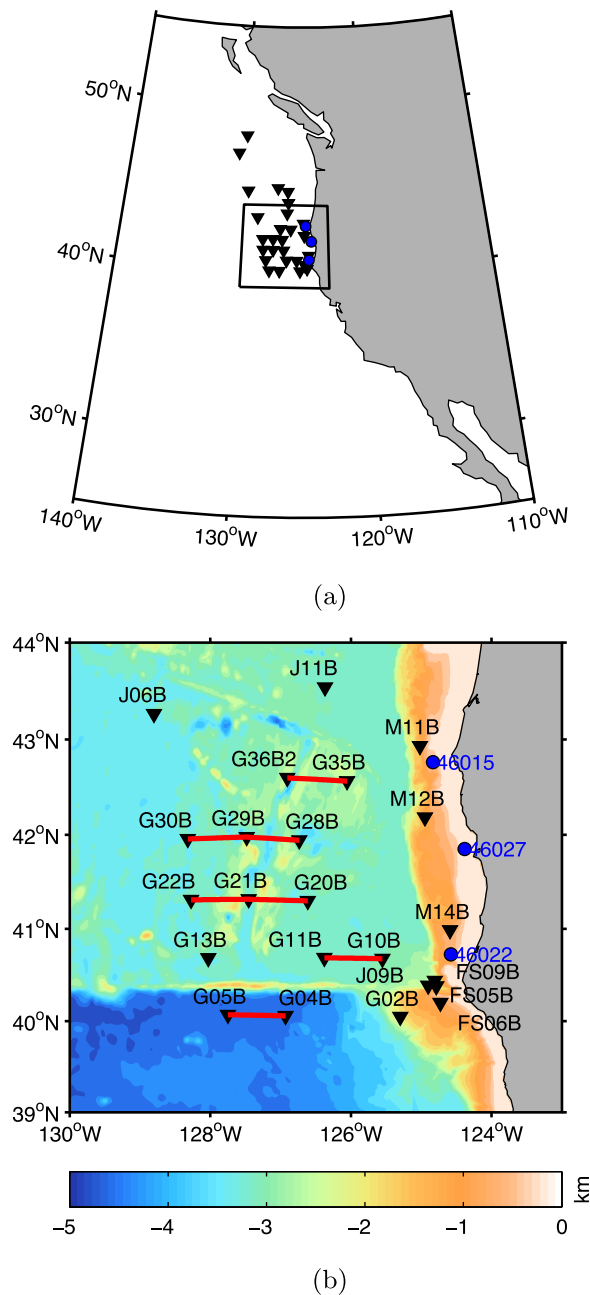


Figure 1. (a) DPG stations of the Cascadia array shown by inverted triangles. Only stations that returned usable data over the whole data period are shown. (b) Enlargement of the boxed region of Figure 1a, also showing bathymetry. Red lines connect east-west-orientated stations (azimuths of 265° – 275°). National Data Buoy Center wave buoys 46015, 46022, and 46027 are marked by the blue circles and labeled.

because previous studies have found a high correlation between H_s and infragravity wave height in shallow water [Herbers *et al.*, 1995b]. In addition, we calculated $\alpha H_s T_{m0,-2}^2 \sqrt{\frac{g}{D}}$ for each buoy where $g = 9.81 \text{ m s}^{-2}$, D is water depth (m), and α is a dimensional constant with units of s^{-1} , because this parameter has been found to improve the correlation between infragravity waves and short-wave conditions [Arduin *et al.*, 2014]. With $\alpha = 12 \times 10^{-4} \text{ s}^{-1}$, the parameter empirically models the observed free infragravity wave height [Arduin *et al.*, 2014; Rawat *et al.*, 2014]. For our purposes, the value of α does not matter as we are interested in the relative change of infragravity wave generation with short-wave conditions rather than

IRIS Data Management System (<http://ds.iris.edu/ds/nodes/dmc/data/types/>). The array consisted of 39 DPGs between depths of 107 and 4462 m offshore of the Pacific Northwest of the U.S. (Figure 1). The locations were considered far enough offshore (50–500 km) to be removed from the effects of infragravity edge waves at the coast, which are trapped within a few hundred meters of the shore [Webb *et al.*, 1991].

Monthly spectra of the records were used to identify bad data. In total, 29 stations returned usable data over the whole data period and these stations were used in the study. The station locations are listed in supporting information Table S1. For most of our analysis we exclude the most northerly stations (above 44°N), which fall outside the main cluster of stations.

The daily pressure records were band pass filtered between 0.002 and 0.45 Hz using a second-order Butterworth filter prior to decimation to 1 Hz, then detrended and tapered.

In order to characterize local infragravity wave generation we also examined near-shore short-wave parameters using data from the National Data Buoy Center's data buoys 46015, 46022, and 46027 (<http://www.ndbc.noaa.gov>), which are also shown in Figure 1. Daily significant wave height, H_s , and average wave period, $T_{m0,-2}$, were calculated for each buoy from the daily average spectra as follows:

$$H_s = 4\sqrt{m_0}, \quad (1)$$

$$T_{m0,-2} = \sqrt{\frac{m_0}{m_2}}, \quad (2)$$

$$m_n = \sum_{fl}^{fu} f^n S(f) d(f), \quad (3)$$

where f is frequency in Hz, $S(f)$ is the nondirectional wave spectrum, $d(f)$ is the bandwidth of each frequency band, $fl = 0.0325 \text{ Hz}$, and $fu = 0.4850 \text{ Hz}$. We use H_s as a proxy for local infragravity wave generation

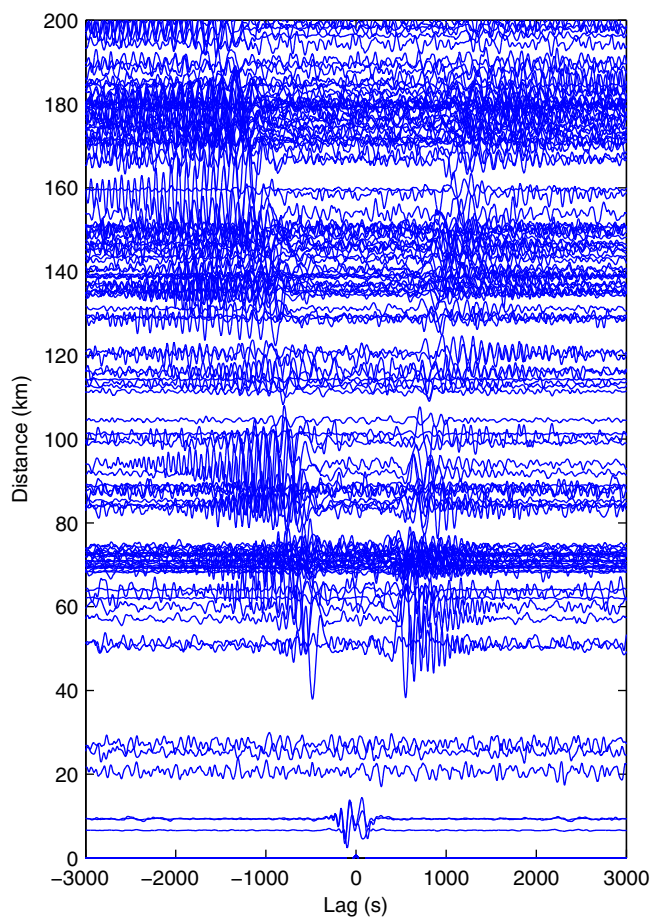


Figure 2. Stacked cross-correlation functions, band pass filtered between 60 and 500 s.

0.0080, 0.0067, 0.0057, and 0.0050 Hz corresponding to periods of 100, 125, 150, 175, and 200 s which covered the main infragravity band. The differential pressure gauges were uncalibrated, so each cross-correlation function was normalized by the maximum of its envelope. Figure 3 shows examples of these band-pass-filtered cross-correlation functions.

Asymmetry of the cross-correlation functions gives information on the direction of infragravity wave propagation across the array. For example, if energy travels from Station 1 to Station 2, the time series at Station 2 will lag the time series at Station 1 by t_1 seconds, where t_1 is the time it takes for energy to travel between the two stations, and a peak in the cross-correlation function at t_1 will result. Likewise, if energy is traveling from Station 2 to Station 1, the time series at Station 1 will lag Station 2 by t_1 , resulting in a peak at $-t_1$ in the cross-correlation function. If energy is traveling perpendicular to the Station 1 to Station 2 alignment, a peak at zero lag would be expected, as both stations receive the signal at the same time. Two methods were used to combine the information contained in all the individual cross-correlation functions from the array: backprojection and beamforming.

Beamforming did not require calculation of unique travel time grids for each frequency, as was necessary for backprojection, so it allowed us to examine directionality over many frequencies, and was more appropriate for analyzing temporal changes in wave propagation over the array from sources outside of the array. However, due to uncertainties about the quality of beamforming over varying bathymetry, backprojection was used to verify the beamforming results, and was useful for examining sources along the coast close to the array.

2.2. Backprojection

Backprojection of the infragravity wave energy allows us to examine the spatial distribution of wave generation inside and outside of the array and to determine the direction of energy propagation across the array.

absolute wave heights, but we used $\alpha = 12 \times 10^{-4} \text{ s}^{-1}$ so that the modeled infragravity wave heights can be compared with other studies. We used both these measures, H_s and $\alpha H_s T_{m0,-2}^2 \sqrt{\frac{g}{D}}$, as proxies for local infragravity wave generation, and we averaged H_s and $\alpha H_s T_{m0,-2}^2 \sqrt{\frac{g}{D}}$ over the three wave buoys.

2.1. Cross Correlation

A cross-correlation function was computed between each DPG station pair on each day to aid in identifying coherent signals between each station pair. A stack over the data period was computed by summing the daily cross-correlation functions to get a sense of the long-term average wavefield (Figure 2). Each cross-correlation function was band pass filtered to a central frequency ± 0.0015 Hz (a wider range was found to make the records too spiky, and a narrower range too smooth, to identify the main peaks), and the envelope of the signal was calculated using a Hilbert transform. The central frequencies used were 0.0100,

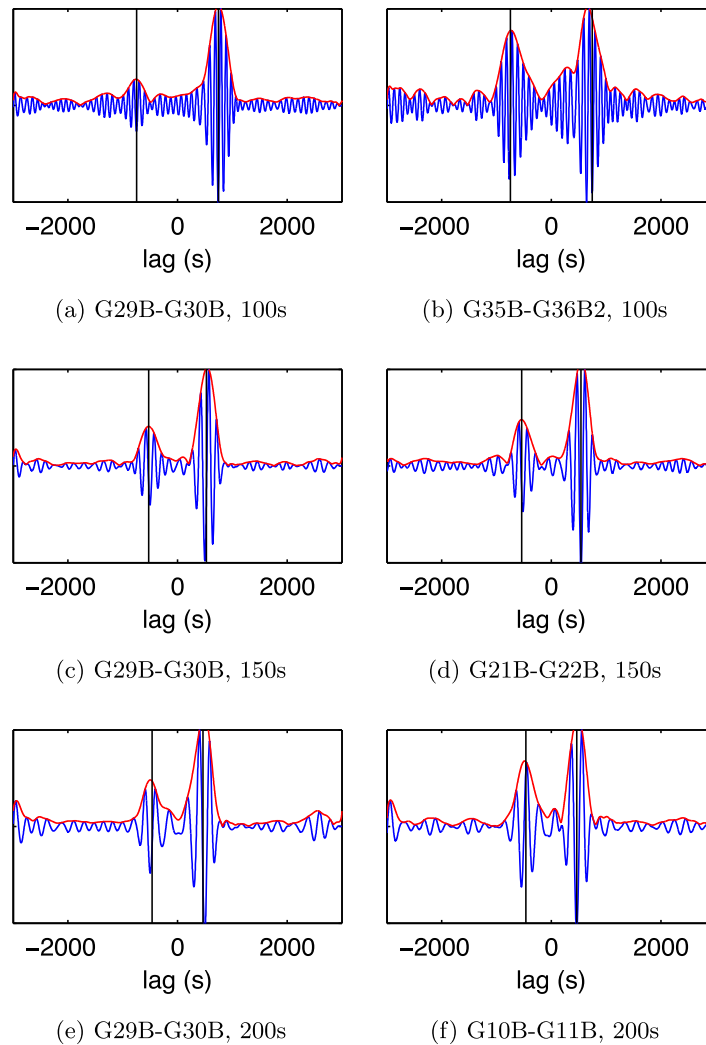


Figure 3. Examples of stacked cross-correlation functions for east-west-aligned station pairs filtered to (top row) 100 s, (middle row) 150 s, and (bottom row) 200 s. Vertical lines are plotted at \pm the theoretical group travel time t_1 between the two stations for an infragravity wave at the given period traveling along the direct raypath between the two stations. Positive lags represent waves propagating from Station 1 to Station 2, and in all these cases Station 2 is furthest offshore.

For each frequency of interest, f , the enveloped cross-correlation functions were backprojected onto a spatial grid of latitude φ and longitude γ using a method similar to that used by *Harmon et al.* [2012] and *Brzak et al.* [2009], and given in equation (4):

$$P(f, l) = \sum_{n=1}^N W_n(f) \text{env}(C_n(f, T_n(f, l))) \quad (4)$$

P is the backprojection as a function of frequency and location index l , (φ_l, γ_l) , where l is the index of each unique latitude and longitude point on our spatial grid (1, 2, ..., L grid points). $\text{env}(C_n)$ is the enveloped band-pass-filtered cross correlation (with center frequency $f \pm 0.0015$ Hz) for station pair n . The envelope was calculated using a Hilbert transform, and the maximum value for the envelope was normalized to 1. W_n is a weighting coefficient for station pair n , described below, to reduce the effect of array geometry on the projection. For an unweighted backprojection, $W_n = 1$ for all n and f . T_n is the theoretical group lag time for station pair n for a hypothetical source at l with frequency f . T_n is calculated using

$$T_n(f, l) = t_i(f, l) - t_j(f, l), \quad (5)$$

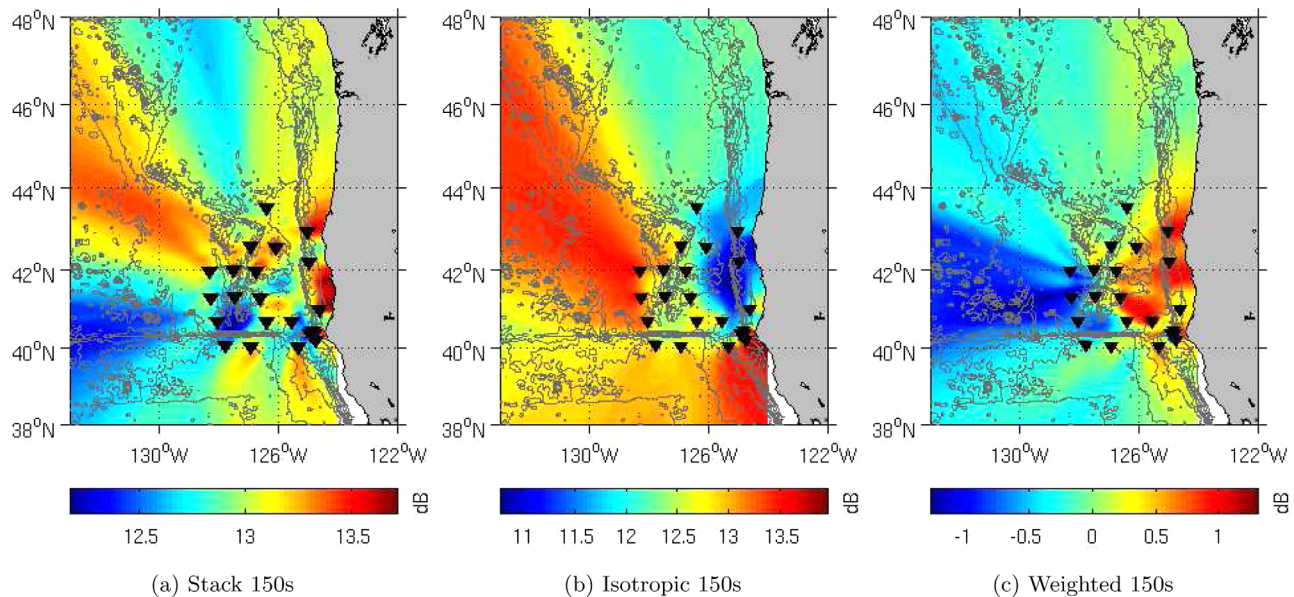


Figure 4. Backprojection of September 2012 to May 2013 stack at 150 s. (a) Backprojection of stack. (b) Backprojection for isotropic source distribution. (c) Weighted stack.

where $t_i(t_j)$ is the group travel time from the source at l with frequency f to station $i(j)$ of the station pair. Group travel times between the source and station are minimum direct travel times calculated using a ray theoretical approach following *Harmon et al.* [2012]. This approach is more accurate than a calculation from interstation distance/average group velocity along the great circle path between the two stations, as it takes into account bathymetry and the effects of nongreat circle propagation paths. $t_i(t_j)$ were calculated in the following way: First, group velocity of infragravity waves at each frequency of interest at each grid point, $v_g(f, l)$, was calculated using ETOP01 bathymetry [*Amante and Eakins, 2009*] and the dispersion relation:

$$\omega^2 = gk \tanh(kh), \quad (6)$$

$$v_g = \frac{\partial \omega}{\partial k}, \quad (7)$$

where $\omega = 2\pi f$ = angular frequency (radians per second), g = acceleration due to gravity (m s^{-2}), k = wavenumber (radians per m), h = water depth (m), and v_g = group velocity (m s^{-1}).

Second, the group velocity grids $v_g(f, l)$ and station locations were input into an Eikonal travel time solver [*Rawlinson and Sambridge, 2004*] which output travel times, $t(f, l)$, from each station to each grid point at each frequency of interest.

To obtain our backprojection $P(f, l)$, we sum the envelopes of the individual band-pass-filtered cross correlations, multiplied by W , at their respective travel time for hypothetical source at l (equation (4)).

Backprojection was computed over a spatial grid of $35^\circ\text{N} < \varphi < 50^\circ\text{N}$, $135^\circ\text{W} < \gamma < 124^\circ\text{W}$ at a spatial resolution of 0.0167° (1 arc min) and at frequencies of 0.0100, 0.0080, 0.0067, 0.0057, and 0.0050 Hz (100, 125, 150, 175, and 200 s). Daily cross correlations became less clear at station separation distances below 50 km and above 120 km, so we only used station pairs within this range (shown in supporting information Figure S1). The output of the backprojection technique is a map for each frequency, as shown in Figure 4a.

2.2.1. Backprojection for Isotropic Source Distribution

In order to be certain that the backprojection results were not an artifact of the array geometry, we calculated what the backprojection results would be if the array was subjected to an isotropic wavefield. Backprojection for an isotropic source distribution, $I(f, l)$, was computed from the theoretical cross-correlation function, $R(f, t)$, which has two symmetrical impulses at the positive and negative lags corresponding to the group arrival time of the raypath between the two stations for the given frequency. The theoretical isotropic cross correlation for each station pair (band pass filtered, enveloped, and normalized to a maximum of 1) can then be backprojected using equation (4) but replacing C_n with R_n and using $W = 1$:

$$I(f, l) = \sum_{n=1}^N W_n(f) \text{env}(R_n(f, T_n(f, l))). \tag{8}$$

From this, we can see which locations the array would illuminate as sources even if all sources were equal. Figure 4b shows the isotropic response for a period of 150 s.

2.2.2. Backprojection Weighting

The theoretical isotropic cross correlations were also used to calculate a weighting coefficient W_n for each unique station pair ($n = 1, 2, \dots, N$ station pairs) for the backprojection using a least squares regression, seeking to minimize equation (9) below [Widrow et al., 1967; Applebaum and Chapman, 1976]:

$$\min_w \|G \cdot W - P\|_2^2, \quad x \geq 0. \tag{9}$$

$P_l = 1$ for each unique latitude and longitude point on our map ($l = 1, 2, \dots, L$ location points). This characterizes an ideal isotropic backprojection for all sources being equal. G_{ln} contains the isotropic backprojection of each station pair n (i.e., equation (8) before the summation over all station pairs). W_n contains the resulting weighting coefficient for each station pair:

$$G_{ln} = \text{env}[R_n(T_n(l))], \tag{10}$$

$$P = \begin{bmatrix} p_1 \\ p_2 \\ \vdots \\ p_L \end{bmatrix} = \begin{bmatrix} 1 \\ 1 \\ \vdots \\ 1 \end{bmatrix}, \tag{10}$$

$$W = \begin{bmatrix} w_1 \\ w_2 \\ \vdots \\ w_N \end{bmatrix}. \tag{10}$$

The backprojection can then be calculated with the solution W using equation (4) which we call a weighted backprojection. An example is given in Figure 4c.

2.3. Beamforming

Beamforming was another method used to estimate the direction of energy propagation across the array. It is similar to backprojection but gives beamformer output as a function of slowness (reciprocal of velocity) and azimuth rather than location, and identifies waves propagating across the array from outside sources.

At each frequency of interest, we generate our beamformer output, B , as function of angular frequency, ω , group slowness, s , and plane wave back azimuth, θ , in the following way and given in equation (11):

$$B(\omega, s, \theta) = \sum_{n=1}^N \text{env}(C_n(\omega, T_n(s, \theta))). \tag{11}$$

C_n is the observed cross correlation for the station pair n band passed at a center frequency, ω . We generate T_n , a synthetic plane wave group travel time for station pair n , at each slowness and back azimuth of interest. T_n is calculated using

$$T_n(\omega, s, \theta) = s * d_n * \cos(\theta - \phi_n), \tag{12}$$

in terms of interstation distance d_n and azimuth ϕ .

We sum the envelopes (env in equation (11), calculated using a Hilbert transform) of the individual band-pass-filtered cross correlations with a center frequency, ω , at their respective synthetic travel time. We use a Gaussian band-pass filter ($\exp(-\alpha * (\omega - \omega_c)^2 / \omega_c^2)$, where $\alpha = 100.0 * \sqrt{\delta} / 1000$ where δ is

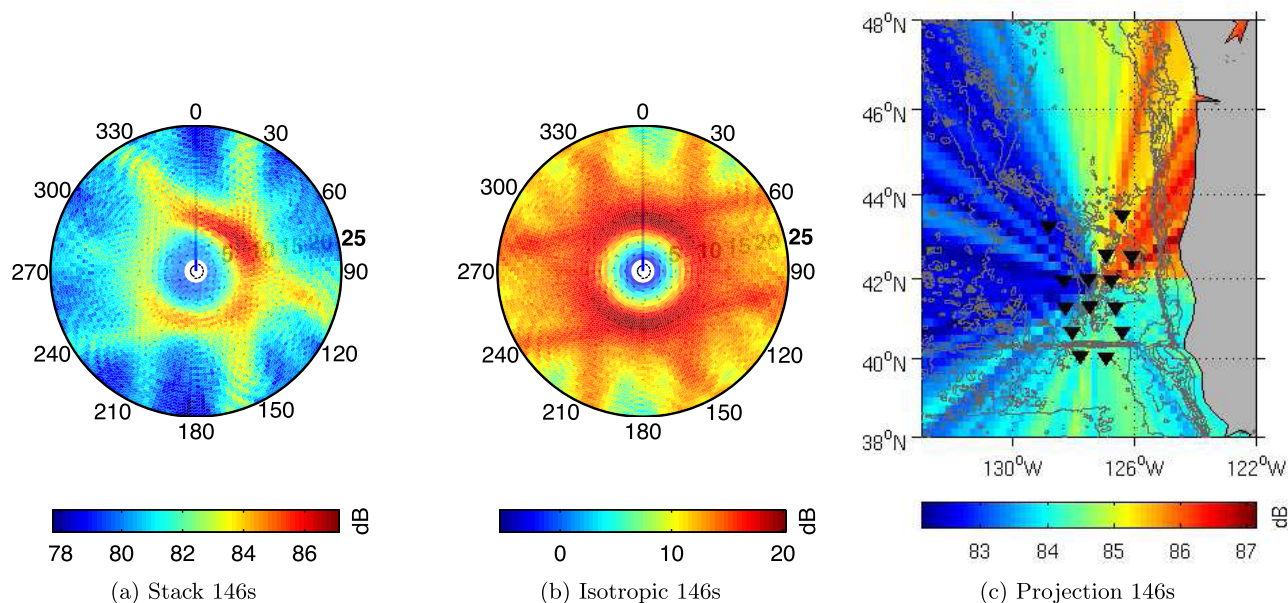


Figure 5. Beamforming of September 2012 to May 2013 stack. (a) Beamforming of stack at 146 s. Radial axis is slowness in s/km, and angular axis is azimuth of wave arrival. (b) Beamforming of isotropic source distribution of plane waves with period 146 s and slowness of 8.22 s/km. (c) Beamform output of Figure 5a at slowness of 8.22 s/km (which is the slowness of maximum beam) projected onto map of Pacific. Rays originate from the array center.

interstation distance, ω is angular frequency, and ω_c is the center angular frequency. We examined from 0.05 to 0.167 Hz, 0 to 360° back azimuth, and 20 to 100 s/km slowness. An example of beamformer output is shown in Figure 5a.

The maximum of the beamformer output identifies the slowness and azimuth of the dominant wavefield for each frequency of interest. However, we note the wavefield may be more complicated than a single plane wave for a given day, with a curved wavefront or multiple components. In the beamformer output, complications present themselves as very broad maxima in azimuth centered on a given slowness or multiple local maxima at the best fitting average array slowness.

The slowness is not so important for our purposes and only verifies that the beamforming is picking up waves that are traveling at the expected velocity for a given frequency and water depth. Our results focus on the azimuth of the dominant wavefield at each frequency of interest.

Our beamforming method works best when there are no large changes in bathymetry (hence slowness) across the array, so we limited the beamforming to stations in deep water west of 126°W where changes in velocity across the array are small (maximum 10% between station pairs).

We also performed the beamforming on theoretical cross correlations for an isotropic distribution of plane waves of a given frequency $R_n(\omega, t)$. $R_n(\omega, t)$ was generated as two symmetrical peaks of value 1 at $t = \pm(s * d_n)$ and 0 at all other t . s was obtained as the slowness of maximum power from our backprojection results for the given frequency. The theoretical isotropic cross correlation R_n for each station pair (band pass filtered, enveloped, and normalized to a maximum of 1) was then input into equation (11) in place of the observed cross correlation C_n . The ideal result in this case would be an equal distribution of energy across all azimuths at the given slowness. Inevitably, the array geometry results in some azimuths being more sensitive than others, but by comparing our results to the isotropic case, we can make sure our results are not an artifact of the array and the processing. The isotropic response at 146 s is shown in Figure 5b.

2.4. Effects of Normalization on Directionality Estimates

Since the amplitudes of the individual DPG's are unknown, we normalized each record by the envelope of each trace prior to cross correlation, effectively only retaining the instantaneous phase information. This

procedure will tend to amplify weaker sources and mute the strongest sources. Therefore, our results will tend to pick out the most coherent wavefield, not necessarily the largest so our directionality estimates are biased in this sense. However, the relative amplitudes on a given cross correlation should accurately represent the relative amount of energy propagating in one direction versus another.

2.5. Calculating Reflection Coefficients

2.5.1. Seaward: Shoreward Wave Propagation

For an offshore station pair aligned perpendicular to a coastline, each side of the cross-correlation function represents either shoreward propagating energy or seaward propagating energy. Therefore, the ratio of the positive and negative enveloped cross correlation at $\pm t_1$ gives the ratio of seaward:shoreward energy propagation. In this case, the coastline lies approximately north-south and so east-west-aligned station pairs (azimuth 265° – 275° or 85° – 95° , shown in Figure 1) were used in the analysis of seaward:shoreward infragravity wave propagation. Again, only station pairs separated by distances >30 and <120 km were used as the quality of the daily cross-correlation functions became much reduced outside this range. This limited the analysis to adjacent stations, and all remaining station pairs were between 60 and 75 km apart.

2.5.2. Assumption of No Local Infragravity Wave Generation

Shoreward propagating infragravity waves were considered to be remote arrivals, while seaward propagating infragravity waves may have been due to reflections at the coast or may have been locally generated “leaky” infragravity waves. In practice, it is difficult to separate the cause of the seaward propagating waves—but previous studies have found that infragravity wave generation is small when either nearshore H_s [Herbers *et al.*, 1995b] or $\alpha H_s T_{m0,-2}^2 \sqrt{\frac{g}{D}}$ [Ardhuin *et al.*, 2014] are small. Here we have used both measures, H_s and $\alpha H_s T_{m0,-2}^2 \sqrt{\frac{g}{D}}$ and assumed that when these were low, the amount of leaky infragravity waves was minimal. In this case, with local generation assumed to be zero, seaward propagation is reflected shoreward incident energy only (see Figure 6). This reflection may involve both specular reflection and scattering, as well as loss of energy through bottom friction and other processes, so the reflection coefficients we calculate contain the net effect of these processes.

Since the amplitude of the reflected wave R equals the amplitude of the incident wave I multiplied by the reflection coefficient r , i.e., $R = Ir$:

$$r^2 = \frac{R^2}{I^2} = \frac{\text{seaward}}{\text{shoreward}}, \quad (13)$$

$$r = \sqrt{\frac{\text{seaward}}{\text{shoreward}}}. \quad (14)$$

Equations (13) and (14) apply to the case illustrated in Figure 6 for a single wave arrival and reflection. The peaks of observed cross-correlations result from waves propagating from multiple directions [Snieder, 2004], but the result still holds and has been shown formally by Wapenaar and Thorbecke [2013] and Godin *et al.* [2014].

This assumption of no local generation at low H_s or $\alpha H_s T_{m0,-2}^2 \sqrt{\frac{g}{D}}$ may not be perfect, so the reflection coefficients calculated should be considered an upper bound.

2.6. Cases of Reflection

To calculate a reflection coefficient, the data were scanned for days when (1) nearshore H_s or $\alpha H_s T_{m0,-2}^2 \sqrt{\frac{g}{D}}$ were low (so that locally generated leaky infragravity waves could be assumed to be negligible and (2) a strong arrival of infragravity energy from the west (240° – 300°) was observed (so that the arrival and reflection are both observable on an east-west-aligned station pair). The 3 days that best matched these conditions were 17 January 2013, 18 January 2013, and 11 May 2013. These days were analyzed along with another 2 days, 25 October 2012 and 4 April 2013, when arrivals from the west were present but less clear, and H_s and $\alpha H_s T_{m0,-2}^2 \sqrt{\frac{g}{D}}$ were (mostly) higher.

For each of the 5 days, the reflection coefficient was calculated from each east-west station pair using equation (14). Values for seaward and shoreward infragravity energy were taken as the peak in the enveloped cross-correlation function at around $\pm t_1$. To account for a wave arrival slightly oblique ($\pm 30^\circ$) to the station

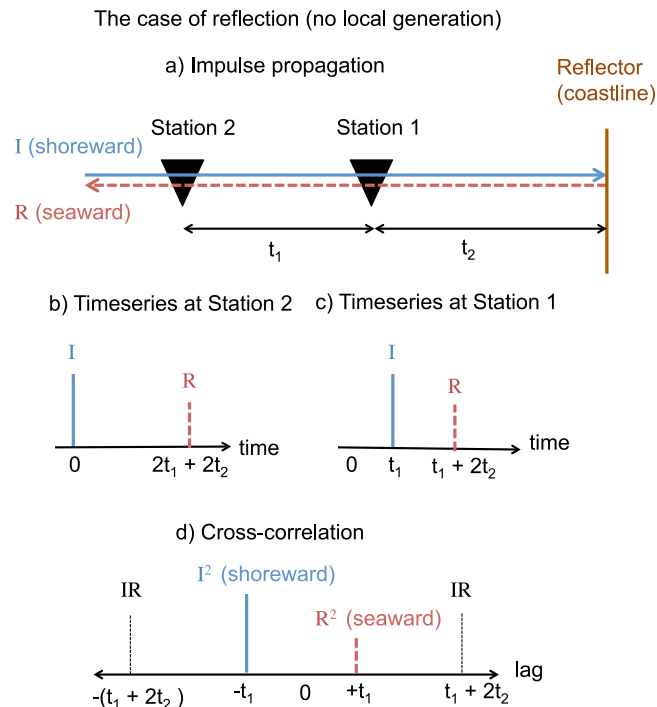


Figure 6. (a) A simple impulse (I) propagates shoreward toward the coastline at normal incidence, passes through Station 2 and Station 1, gets reflected, and propagates back seaward (R). t_1 is the travel time between Station 1 and Station 2. t_2 is the travel time between Station 1 and the coast. (b) The time series observed at Station 2. (c) The time series observed at Station 1. (d) Cross correlation of records at Station 1 and Station 2.

pair alignment (270°) and velocity errors/scattering, which would result in a peak slightly off $\pm t_1$, the maximum value in a 200 s window around $\pm t_1$ was used as the peak. Varying this window between 100 and 300 s made very little difference to the results.

3. Results

3.1. Infragravity Wave Energy and Directionality

Figure 2 shows the stacked cross correlations filtered between 60 and 500 s, and Figure 3 shows examples from east-west-aligned station pairs filtered to 100, 150, and 200 s. Peaks at \pm the theoretical travel time t_1 of an infragravity wave group between the two stations confirms that over the year there is coherent infragravity wave energy propagating both seaward and shoreward, with more going seaward.

From backprojection and beamforming, the dominant source of infragravity

energy was found to be from the coastline to the east/northeast, consistent with local generation, as seen in Figures 4c and 5c (plots for other periods are similar can be seen in supporting information Figures S2 and S3). Backprojection (Figure 4c) highlighted the stretch of coastline between 40°N and 44°N as the dominant source, while beamforming (Figure 5c) identified the region between 42°N and 46°N as the main source. The differences are small but may be due to the fact that backprojection used additional stations nearer the coast and was weighted to remove effects to array geometry. There was however a notable change in direction with time of year (Figure 7). The source to the east/northeast dominated from mid-September through to March, but in April and continuing through May the dominant source shifted to the south, coinciding with the switch to austral winter and perhaps indicating a switch to a remote infragravity wave source.

The change in source direction to the south was accompanied by a reduction in power at infragravity wave frequencies (Figure 8a). Power showed a positive correlation with local short-wave H_s and $\alpha H_s T_{m0,-2}^2 \sqrt{\frac{g}{D}}$ (Figures 8b–8e), indicating the importance of leaky infragravity waves generated at the local coastline to infragravity power offshore in this part of the ocean. Scatter in the relationship could be partly due to remote arrivals. For example, power on 17 January 2013, 18 January 2013, and 11 May 2013 (marked by the black crosses in Figures 8d and 8e) was higher than expected for the local H_s or $\alpha H_s T_{m0,-2}^2 \sqrt{\frac{g}{D}}$, probably due to the infragravity arrival observed from the west.

3.2. Reflection of Infragravity Waves

The infragravity seaward:shoreward ratio was calculated for each daily cross correlation in the record. Throughout most of the record, the infragravity seaward:shoreward ratio was >1 (i.e., offshore propagation). A ratio >1 cannot be explained by incident arrivals and their reflections, but again indicates that for most days of the record the deep water infragravity waves were generated at the local coastline to the east. As with infragravity power (Figures 8d and 8e) the seaward:shoreward ratio increased as significant wave height H_s and $\alpha H_s T_{m0,-2}^2 \sqrt{\frac{g}{D}}$ increased at the coast (Figures 9a and 9b). Again, scatter in the relationship

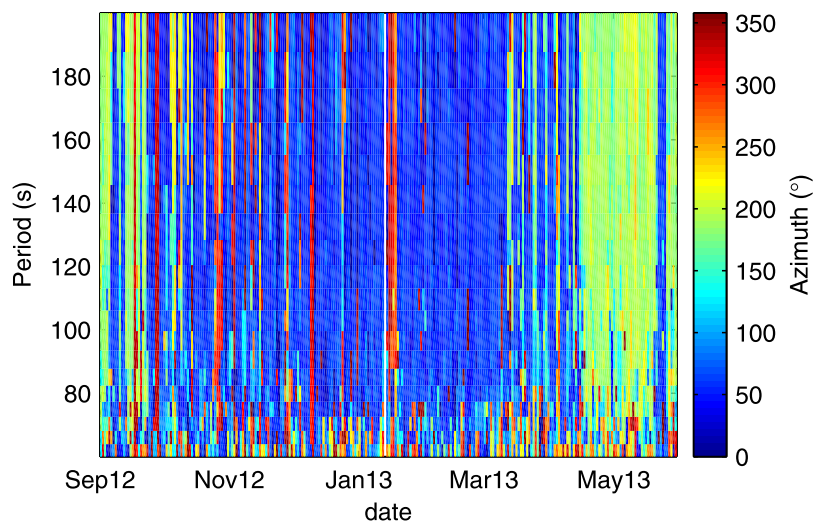


Figure 7. Direction of maximum beam power, September 2012 to May 2013.

may be caused by the shoreward propagating infragravity waves (which have no reason to correlate with H_s or $\alpha H_s T_{m0,-2}^2 \sqrt{\frac{g}{D}}$) as well as the likely imperfect relationship between H_s or $\alpha H_s T_{m0,-2}^2 \sqrt{\frac{g}{D}}$ and seaward propagating waves. With the data binned according to H_s or $\alpha H_s T_{m0,-2}^2 \sqrt{\frac{g}{D}}$ the correlation with seaward:shoreward energy became much clearer (Figures 9a and 9b, red circles). At H_s of about 4 m and below, or $\alpha H_s T_{m0,-2}^2 \sqrt{\frac{g}{D}}$ of about 0.05 m and below, the relationship between H_s and $\alpha H_s T_{m0,-2}^2 \sqrt{\frac{g}{D}}$ and the seaward:shoreward ratio was approximately linear. For H_s , a linear regression calculated from the first four binned data points (which all had standard error of ≤ 0.14) had a slope of $0.69 \pm 0.04 \text{ m}^{-1}$ and intercept of 0.21 ± 0.10 . For $\alpha H_s T_{m0,-2}^2 \sqrt{\frac{g}{D}}$, the first five binned data points all had standard error of ≤ 0.10 and had a slope of $33.27 \pm 1.48 \text{ m}^{-1}$ and intercept of 0.55 ± 0.04 . The square root of the intercept is an estimate of the reflection coefficient if the seaward:shoreward ratio is linear, therefore giving an estimate of $r \approx 0.49 \pm 0.29$ for H_s or $r \approx 0.74 \pm 0.06$ for $\alpha H_s T_{m0,-2}^2 \sqrt{\frac{g}{D}}$. At higher H_s or $\alpha H_s T_{m0,-2}^2 \sqrt{\frac{g}{D}}$, the data suggested a potential leveling off of seaward-propagating (leaky) infragravity waves, but the number of data points at these higher values was limited.

Figure 10 shows one of the examples when H_s and $\alpha H_s T_{m0,-2}^2 \sqrt{\frac{g}{D}}$ were low (Table 1), and a strong infragravity arrival from the west was observed. The reflection coefficient was calculated from each of the seven east-west-aligned station pairs on this day, at periods of 100, 125, 150, 175, and 200 s. Some examples of cross correlations on this day, from which the reflection coefficient was calculated, are shown in Figure 11. The reflection coefficient calculated varied between the different station pairs. Each cross in Figure 12a shows the reflection coefficient calculated for each station pair at each period. The mean varied between 0.83 at 100 s and 0.51 at 200 s, with a mean over all periods and station pairs of 0.66. A visual inspection of the cross-correlation functions found that for some station pairs the two peaks were not evident at all, and so a calculation based on the values at these two peaks was essentially meaningless (see supporting information Figure S5 for some examples of unclear correlations). For this reason, any unclear cross correlations were discarded, and the results were replotted (supporting information Figure S6a). In this case, the mean varied between 0.90 at 100 s to 0.59 at 200 s, with a mean over all periods of 0.71 (the mean at each period is plotted in Figure 13). It is understood that this approach risks a bias toward larger reflection coefficients, although an inspection of the differences found that overall both anomalous low and high values were removed, and the remaining data points became less scattered.

The reflection coefficient was calculated in the same way for the other four dates (25 October 2012, 17 January 2013, 4 April 2013, and 11 May 2013) when $H_s < 2 \text{ m}$ (and $\alpha H_s T_{m0,-2}^2 \sqrt{\frac{g}{D}} < 0.03 \text{ m}$) and

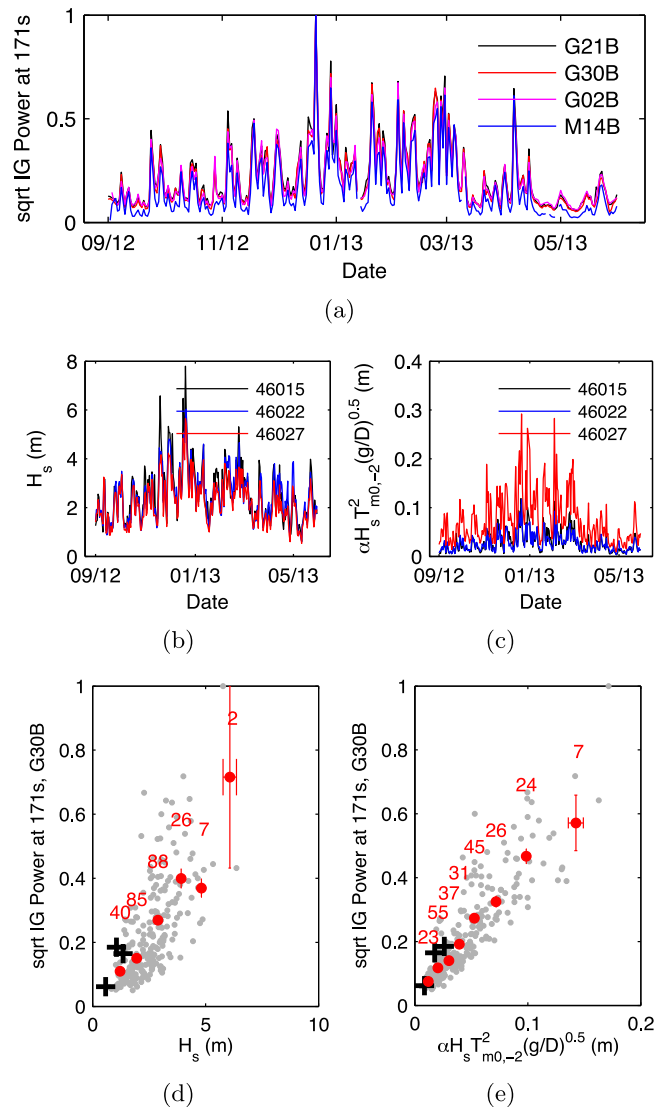


Figure 8. (a) Infragravity (IG) power at 171 s at stations G21B, G30B, G02B, and M14B. Each time series has been normalized by its maximum value. (b) Daily significant wave height H_s (m) at buoys 46015, 46022, and 46027. (c) $\alpha H_s T_{m0,-2}^2 \sqrt{g/D}^{0.5}$ (m) at buoys 46015, 46022, and 46027. (d) Mean H_s versus IG power at G30B. Gray points show daily H_s (averaged over the three buoys) versus IG power. The daily data points were binned into eight bins according to H_s , with centers of 1, 2, 3, 4, 5, 6, 7, and 8 m, and the red points mark the mean of each bin. Error bars have a length of two standard errors (1 SE positive and 1 SE negative), and the corresponding numbers give the number of data points in that bin. 17 January 2013, 18 January 2013, and 11 May 2013 are marked by the black crosses. (e) Same as Figure 8d but using $\alpha H_s T_{m0,-2}^2 \sqrt{g/D}^{0.5}$ and bin centers of 0.010, 0.020, 0.030, 0.040, 0.050, 0.075, 0.100, and 0.150 m.

westerly arrivals were observed (Figures 12b–12e and 13). The number of stations considered to have clear cross correlations on these other 4 days was generally less than on 18 January 2013 (numbers along bottom of figures in supporting information Figure S6). In particular, the arrivals on 25 October 2012 and 4 April 2013 were much less clear and not over all periods (see supporting information Figure S4 for backprojection plots). Therefore, we focus on the “best cases” of 17 January 2013, 18 January 2013, and 11 May 2013.

The mean reflection coefficient at each period from each of the 5 days (Figures 12a–12e) is plotted together in Figure 12f, and the means from supporting information Figures S6a–S6e are plotted together in Figure 13. The means were closely matched, especially for 18 January 2013 and 11 May 2013, in Figure 13. It is difficult to explain why the values obtained for the 17 January 2013 are the lowest obtained despite not having the lowest H_s , or $\alpha H_s T_{m0,-2}^2 \sqrt{g/D}^{0.5}$ (Table 1). The mean reflection coefficient obtained over the three best cases

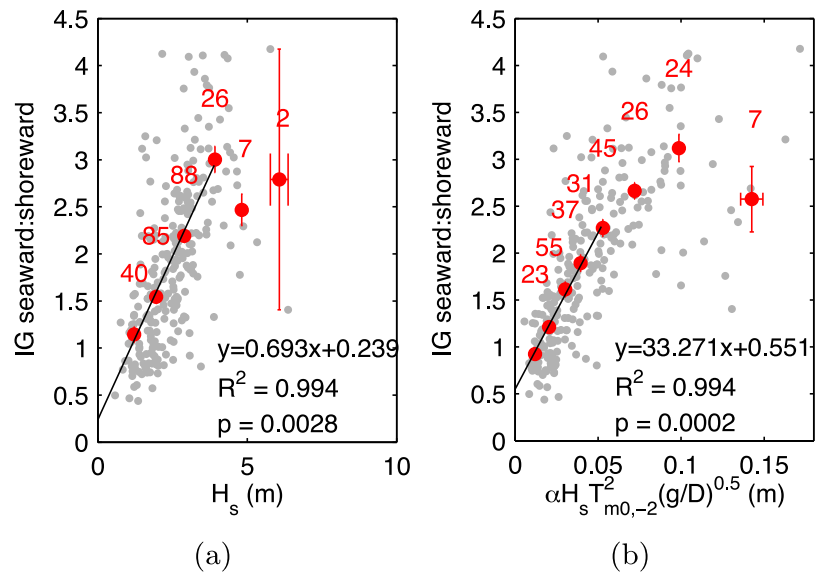
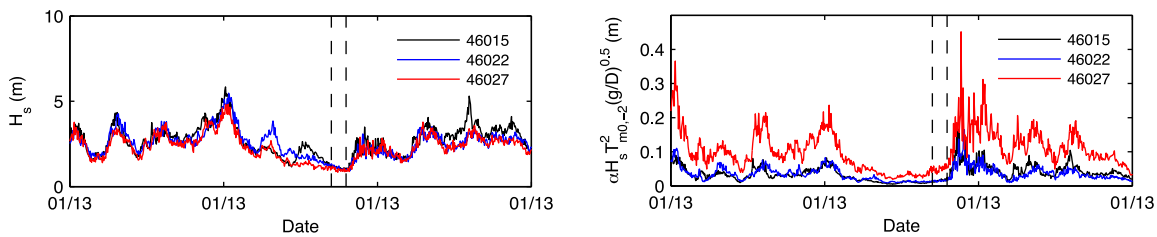
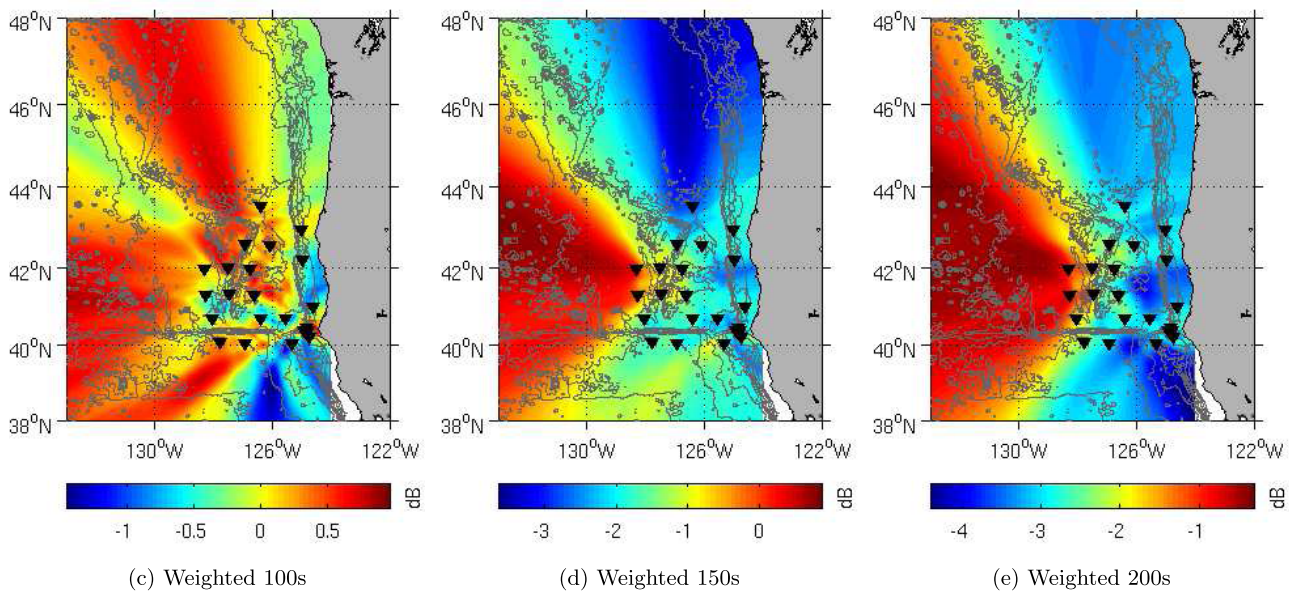


Figure 9. Same as Figures 8d and 8e but H_s and $\alpha H_s T_{m0,-2}^2 \sqrt{\frac{g}{D}}$ versus daily seaward:shoreward energy. Daily seaward:shoreward energy was calculated as the mean from the seven east-west station pairs over all periods 100–200 s. A linear regression was calculated through the first four (for H_s) or five (for $\alpha H_s T_{m0,-2}^2 \sqrt{\frac{g}{D}}$) binned points and the equation of best fit, R^2 value, and p value are shown.



(a) H_s

(b) $\alpha H_s T_{m0,-2}^2 \sqrt{\frac{g}{D}}$



(c) Weighted 100s

(d) Weighted 150s

(e) Weighted 200s

Figure 10. (a) H_s and (b) $\alpha H_s T_{m0,-2}^2 \sqrt{\frac{g}{D}}$ at buoys 46015, 46022, and 46027 during January 2013. 18 January is bounded by the dashed lines. Backprojection on 18 January at (c) 100 s, (d) 150 s, and (e) 200 s shows the westerly infragravity wave arrival.

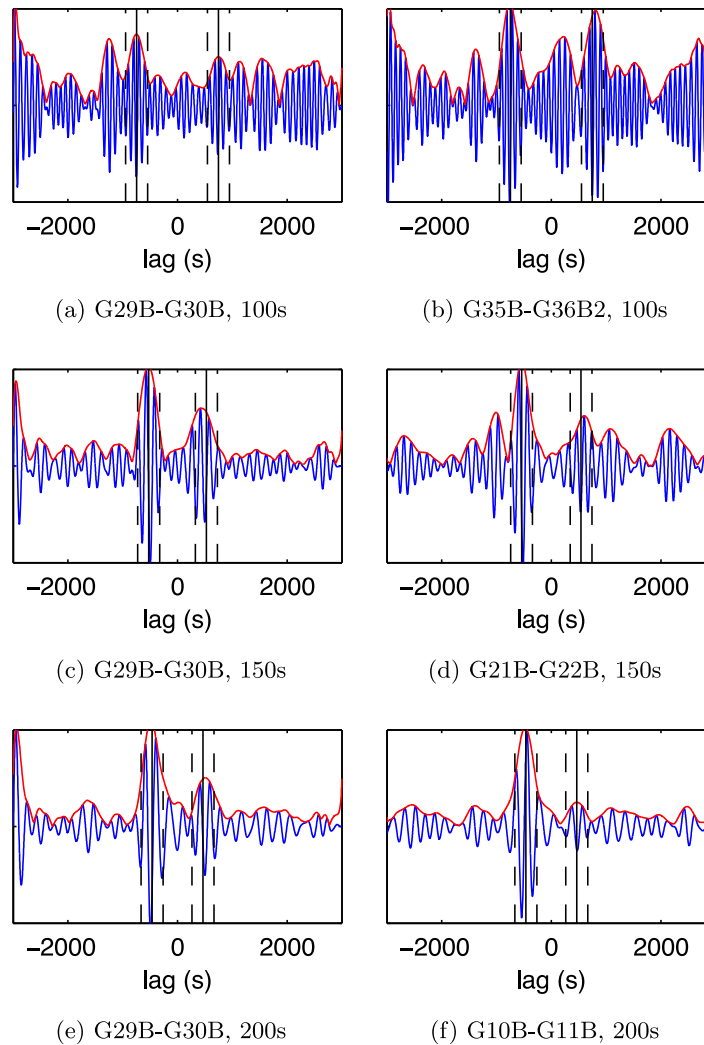


Figure 11. Same as Figure 3 except for 18 January 2013. The ratio of the positive to negative peak was used to calculate the seaward:shoreward energy ratio for each station pair. The peak was taken as the maximum of the envelope (red line) in a 200 s window either side of the theoretical group travel time (shown by the dashed vertical lines).

of 17 January 2013, 18 January 2013, and 11 May 2013 is given in Table 2, for both the calculations where all seven station pairs' cross correlations were used (Figure 12) and for the calculation using only selected clear cross correlations (Figure 13). The means were 0.65 ± 0.02 and 0.66 ± 0.02 , respectively. These estimates lie within the estimates of r from the linear regressions of seaward:shoreward energy with H_s and $\alpha H_s T_{m0,-2}^2 \sqrt{\frac{g}{D}}$ which are also shown in Table 2.

4. Discussion

The dominant infragravity wave sources found here are in agreement with previous studies. The northwest coast of America has consistently showed up as a source of infragravity waves [Webb *et al.*, 1991; Rhie and Romanowicz, 2006; Aucan and Ardhuin, 2013; Rawat *et al.*, 2014]. In general, the eastern boundaries of basins provide stronger sources of infragravity waves than western boundaries due to larger wave heights and wave periods incident on these coasts [Rawat *et al.*, 2014]. However, a recent study by Crawford *et al.* [2015] on deep ocean infragravity waves in the Atlantic has shown that other factors such as short-wave incidence angle or spread and coastal morphology may be more important for infragravity wave generation than wave heights and periods. This study has shown some rare examples where infragravity waves arrived from the western side of the Pacific.

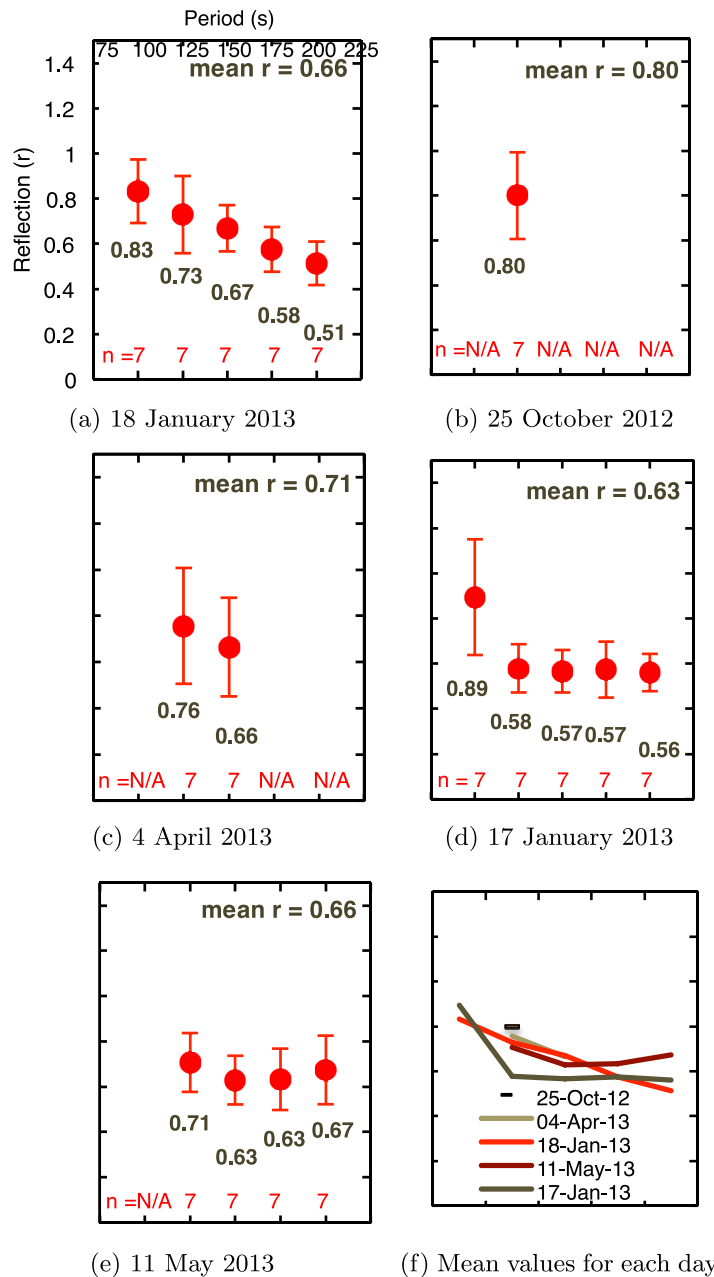


Figure 12. Values of r (\sqrt{IG} seaward : shoreward) obtained from east-west station pairs on (a) 18 January 2013, (b) 25 October 2012, (c) 4 April 2013, (d) 17 January 2013, and (e) 11 May 2013. The red points mark the mean value of r from the seven east-west station pairs at each period, with error bars of two standard deviations (1 SD positive and 1 SD negative). The number of station pairs used in the calculation of the mean is given along the bottom of the plot. N/A means no estimate of r was made because backprojection showed no clear arrival from the west for this period. The mean value of r over all periods is given by the number in the top right corner of each plot. (f) The mean values at each period from Figures 12a–12e. The axes for all plots are equal to those given for Figure 12a.

The results suggest that infragravity waves that propagated west to east across the Pacific Ocean reflected at the North American Pacific coastline strongly. Perhaps the main limitation of the method used is that is problematic to distinguish between reflected infragravity waves and locally generated infragravity waves. Here the reflection coefficient was estimated by assuming that there were no locally generated infragravity waves on the days investigated because nearshore significant wave height H_s or the parameter $\alpha H_s T_{m0,-2}^2 \sqrt{\frac{g}{D}}$ was low. An alternative method which extrapolated the observed trend of the seaward:shoreward ratio with H_s and $\alpha H_s T_{m0,-2}^2 \sqrt{\frac{g}{D}}$ to zero complemented the results obtained on the individual days investigated.

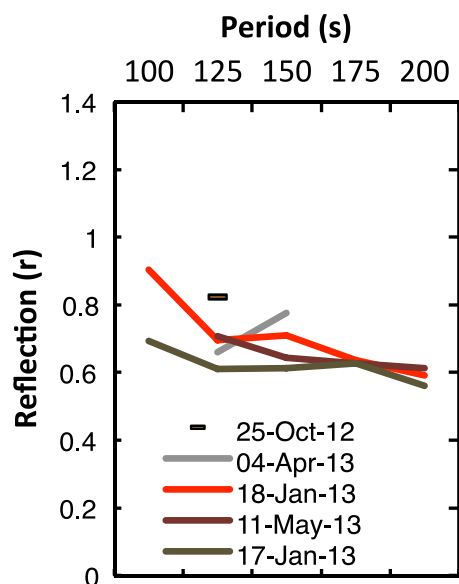


Figure 13. Same as Figure 12f but only using selected clear cross correlations.

here, is by identifying a peak in energy that arrives at a greater lag than the main arrival ($t_1 + 2t_2$ peak labeled IR in Figure 6d). This peak has not been clearly identified in this data set. This might be because the schematic in Figure 6 is too simple for the real complicated wavefield. The complexity of the wavefield can be seen by the early arrivals and multiple late arrivals in the cross correlations (Figures 3 and 11), indicating waves propagating obliquely to normal incidence and multiple reflections, respectively. The IR peak would not be clear or symmetrical if reflection occurred from a source unaligned with the station pair, from multiple sources, or occurred gradually over a large geographical area (such as the continental shelf). The beam-forming output does show a late arrival in the direction that would be expected from a reflection, but the isotropic responses in Figure 5 suggest that this is due to aliasing by the array geometry. However, a good example of this reflection peak can be seen in the data of Harmon *et al.* [2012] for pressure gauges southwest of Sumatra, which were dominated by remote arrivals rather than local generation. The stacked cross correlation between their stations 42 and 45 shows symmetrical secondary peaks at -2000 and $+2000$ s lags (supporting information Figure S8a). A quick calculation of the reflection coefficient from the ratio of the IR peak to the I^2 peak gives r of approximately 0.3, which is much lower than that found here, but is not based only on arrivals at normal incidence to the coast. This result may indicate that reflection coefficients depend strongly on the bathymetry and configuration of coastlines. Indeed, if all coastlines reflected at approximately 0.7, then infragravity energy in the middle of the ocean would be substantially higher than a case with no reflection. However, Webb *et al.* [1991] found little infragravity waves originating from large parts of the Pacific, which led them to suggest that reflection from coastlines is small. This perhaps suggests that the North American Pacific coastline is an example of a particularly strong reflector for infragravity waves reflecting at normal incidence to the coast (as indeed it is also a strong source [Arduin *et al.*, 2014]).

The lag time of this late arrival (IR peak at $t_1 + 2t_2$) can also offer information on where the reflection occurs—whether at the continental slope or at the shoreline, or a combination of both. A backprojection of

One approach to tackling the problem of locally generated infragravity waves might be to use calibrated pressure gauges (only uncalibrated gauges were available in this study). Then, the expected seaward propagating infragravity wave energy for a particular sea state could be estimated from an empirical model between sea state and infragravity wave height, for example such as that described in Arduin *et al.* [2014], and then removed from the observed seaward propagating energy. This would have other problems associated with it such as the accuracy of the model for particular coastlines and sea states. However, it might offer some more insight as to the magnitude of the reflection and allow estimates of reflection to be made on days when wave activity at the coast is larger, so local generation cannot be assumed to be zero. Another approach could be to use modeled infragravity energy for the whole ocean basin [Arduin *et al.*, 2014] and see if there is a mismatch in modeled and observed energy on days when reflection is expected to be large.

Another way to distinguish reflection from local generation, which should be possible with the method used

Table 1. Nearshore Short-Wave Conditions for Days of Westerly Infragravity Arrivals^a

Date	H_s (m)	Average Wave Period $T_{m0,-2}$ (s)	$\alpha H_s T_{m0,-2}^2 \sqrt{\frac{g}{D}}$ (m)	Dominant Wave Period (s)	Dominant Wave Direction (°)
4 Apr 2013	1.83	6.11	0.019	8.37	238
25 Oct 2012	1.63	6.55	0.021	8.84	301
17 Jan 2013	1.36	6.50	0.018	12.90	286
18 Jan 2013	1.06	8.82	0.026	12.90	288
11 May 2013	0.58	6.88	0.009	14.81	213

^aAverage of NDBC wave buoys 46015, 46022, and 46027. Spectra are shown in supporting information Figure S7.

Table 2. Estimates of Reflection Coefficient

	Reflection Coefficient, r	Standard Error	Standard Deviation
All cross correlations from three best cases ^a	0.65 ^b	0.02 ^c	0.17
Subselected cross correlations from three best cases	0.66	0.02	0.13
Regression estimate from H_s	0.49 ^d	0.29	
Regression estimate from $\alpha H_s T_{m0,-2}^2 \sqrt{\frac{g}{D}}$	0.74 ^d	0.06	

^aBest cases are 17 January 2013, 18 January 2013, and 11 May 2013.

^bMean reflection coefficient over east-west stations pairs at periods 100–200 s.

^cStandard deviation/ \sqrt{n} where n is number of cross correlations used in the calculation of mean r .

^dSquare root of intercept shown in Figure 8.

the Sumatra lag onto a $t_1 + 2t_2$ travel time grid (i.e., T_n in equation (4) = $(t_i(f, l) - t_j(f, l)) + 2 * t_j(f, l)$) puts the reflection off the island of Batu at depths of 25–100 m (supporting information Figures S8b and S8c). There are no other studies (that the authors are aware of) that estimate reflection of transoceanic propagating infragravity waves in deep water, and therefore their potential reflection from a continental shelf, but previous studies of infragravity waves in shallow water have calculated reflection at the shoreline. These studies found reflection at the shoreline to be similar or higher to those found here: $r^2 = 0.6 \pm 0.11$ and $r^2 = 0.65 \pm 0.25$ (corresponding to $r = 0.77$ and $r = 0.81$) for two sites in *De Bakker et al.* [2014], or $r^2 = 0.8$ ($r = 0.89$) in *Sheremet* [2002]. If reflection did occur at the shoreline rather than at the shelf, the “reflection coefficient” obtained in deep water would not strictly be only a reflection coefficient, but would contain the effects of dissipation on two crossings of the shelf. Considering dissipation can occur by bottom friction, triad interactions, or breaking [*De Bakker et al.*, 2014] and any reflected waves could become trapped, the reflection coefficients obtained in this study would seem quite large, although perhaps explained by a narrow shelf. On the other hand, the continental shelf is fairly linear (north-south) and it could be because of this that we observe a very coherent reflected wavefield, more than what would be expected for a more irregular shoreline. A simple calculation for long-wave reflection at a step, $r = (1 - \sqrt{h_1/h_0}) / (1 + \sqrt{h_1/h_0})$ from *Lamb* [1932], where we use $h_1 = 100$ m and $h_0 = 3000$ m based on the bathymetry of our study region, gives a value of $r = 0.69$, which is similar to our estimates. Of course, this oversimplifies the problem as the bathymetry is more complex than a simple step, so the agreement may be merely fortuitous. As infragravity waves refract toward normal incidence as they cross the shelf [*Herbers et al.*, 1995a], reflection from the shoreline should depend less on the angle of incidence of the remote arrival than reflection at the continental shelf, and this may be another way to distinguish the location of the reflector.

5. Conclusions

The North American Pacific coastline was found to be the dominant source of infragravity waves observed offshore, although energy and source were found to change seasonally. During northern-hemisphere winter, infragravity wave energy was higher and the waves mostly originated from the nearby coastline to the east/northeast, while during northern-hemisphere summer, energy decreased and arrivals mostly came from the south. The seasonal pattern can be explained by the relationship between infragravity waves and short-period (2–30 s) wave activity. Infragravity wave energy in the deep ocean (i.e., leaky free infragravity waves) increased with short-period wave activity at the coast (indicated by H_s and $\alpha H_s T_{m0,-2}^2 \sqrt{\frac{g}{D}}$), resulting in higher infragravity wave energy during winter when short-period wave activity is highest.

Remote arrivals coming from the west, propagating eastward, were observed but rare. The strength of reflection of these remote arrivals was estimated using the asymmetry of cross-correlation functions calculated between station pairs perpendicular to the coastline. While the method is limited to the assumption of no local infragravity wave generation when short-period wave activity is low, reflection did appear to be strong, with a lower bound estimate of $r = 0.49 \pm 0.29$ (reflection coefficient \pm standard error) and an upper bound estimate of $r = 0.74 \pm 0.06$ for this particular coastline. These results indicate that reflection has the potential to be an important factor to account for infragravity wave energy in the deep ocean.

References

Aagaard, T., and B. Greenwood (2008), Infragravity wave contribution to surf zone sediment transport—The role of advection, *Mar. Geol.*, 251, 1–14, doi:10.1016/j.margeo.2008.01.017.

Acknowledgments

We used data from the Cascadia Initiative array, whose webpage can be accessed at <http://cascadia.uoregon.edu/welcome>. The data are freely available to the public and can be downloaded from the IRIS Data Management Center (<http://ds.iris.edu/ds/nodes/dmc/>). Wave buoy data were obtained from the National Data Buoy Center freely available at <http://www.ndbc.noaa.gov>. J. Neale’s PhD studentship was funded by the U.K. Natural Environment Research Council and the University of Southampton at the National Oceanography Centre, Southampton. We thank three anonymous reviewers for their valuable suggestions.

- Amante, C., and B. Eakins (2009), ETOPO1 1 Arc-Minute Global Relief Model: Procedures, data sources and analysis, *NOAA Tech. Mem. NES-DIS NGDC-24*, Natl. Geophys. Data Cent., Natl. Ocean. Atmos. Admin., doi:10.7289/V5C8276M, accessed 20 Jan 2014.
- Applebaum, S., and D. Chapman (1976), Adaptive arrays with main beam constraints, *IEEE Trans. Antennas Propag.*, *24*(5), 650–662, doi:10.1109/TAP.1976.1141416.
- Arduin, F., A. Rawat, and J. Aucan (2014), A numerical model for free infragravity waves: Definition and validation at regional and global scales, *Ocean Modell.*, *77*, 20–32, doi:10.1016/j.ocemod.2014.02.006.
- Arduin, F., L. Gualtieri, and E. Stutzmann (2015), How ocean waves rock the Earth: Two mechanisms explain microseisms with periods 3 to 300 s, *Geophys. Res. Lett.*, *42*, 765–772, doi:10.1002/2014GL062782.
- Aucan, J., and F. Arduin (2013), Infragravity waves in the deep ocean: An upward revision, *Geophys. Res. Lett.*, *40*, 3435–3439, doi:10.1002/grl.50321.
- Battjes, J. A. (2004), Shoaling of subharmonic gravity waves, *J. Geophys. Res.*, *109*, C02009, doi:10.1029/2003JC001863.
- Bromirski, P. D., O. V. Sergienko, and D. R. MacAyeal (2010), Transoceanic infragravity waves impacting Antarctic ice shelves, *Geophys. Res. Lett.*, *37*, L02502, doi:10.1029/2009GL041488.
- Brzak, K., Y. J. Gu, A. Ökeler, M. Steckler, and A. Lerner-Lam (2009), Migration imaging and forward modeling of microseismic noise sources near southern Italy, *Geochem. Geophys. Geosyst.*, *10*, Q01012, doi:10.1029/2008GC002234.
- Crawford, W., V. Ballu, X. Bertin, and M. Karpytchev (2015), The sources of deep ocean infragravity waves observed in the North Atlantic Ocean, *J. Geophys. Res. Oceans*, *120*, 5120–5133, doi:10.1002/2014JC010657.
- Crawford, W. C., S. C. Webb, and J. A. Hildebrand (1998), Estimating shear velocities in the oceanic crust from compliance measurements by two-dimensional finite difference modeling, *J. Geophys. Res.*, *103*(B5), 9895–9916, doi:10.1029/97JB03532.
- De Bakker, A. T. M., M. F. S. Tissier, and B. G. Ruessink (2014), Shoreline dissipation of infragravity waves, *Cont. Shelf Res.*, *72*, 73–82, doi:10.1016/j.csr.2013.11.013.
- Godin, O. A., N. A. Zabotin, A. F. Sheehan, Z. Yang, and J. A. Collins (2013), Power spectra of infragravity waves in a deep ocean, *Geophys. Res. Lett.*, *40*, 2159–2165, doi:10.1002/grl.50418.
- Godin, O. A., N. A. Zabotin, A. F. Sheehan, and J. A. Collins (2014), Interferometry of infragravity waves off New Zealand, *J. Geophys. Res. Oceans*, *119*, 1103–1122, doi:10.1002/2013JC009395.
- Godin, O. A., N. A. Zabotin, and T. W. Bullett (2015), Acoustic-gravity waves in the atmosphere generated by infragravity waves in the ocean, *Earth Planets Space*, *67*(1), 47, doi:10.1186/s40623-015-0212-4.
- Harmon, N., T. Henstock, M. Srokosz, F. Tilmann, A. Rietbrock, and P. Barton (2012), Infragravity wave source regions determined from ambient noise correlation, *Geophys. Res. Lett.*, *39*, L04604, doi:10.1029/2011GL050414.
- Herbers, T. H. C., S. Elgar, and R. T. Guza (1995a), Generation and propagation of infragravity waves, *J. Geophys. Res.*, *100*(C12), 24,863–24,872, doi:10.1029/95JC02680.
- Herbers, T. H. C., S. Elgar, R. T. Guza, and W. C. O'Reilly (1995b), Infragravity-frequency (0.005–0.05 Hz) motions on the shelf. Part II: Free waves, *J. Phys. Oceanogr.*, *25*, 1063–1079, doi:10.1175/1520-0485(1995)025<1063:IFHMOT>2.0.CO;2.
- Lamb, H. (1932), *Hydrodynamics*, 6th ed., 263 pp., Cambridge Univ. Press, London, U. K.
- Livneh, D. J., I. Seker, F. T. Djuith, and J. D. Mathews (2007), Continuous quasiperiodic thermospheric waves over Arecibo, *J. Geophys. Res.*, *112*, A07313, doi:10.1029/2006JA012225.
- Longuet-Higgins, M. S., and R. W. Stewart (1962), Radiation stress and mass transport in gravity waves, with application to 'surf beats,' *J. Fluid Mech.*, *13*(4), 481–504, doi:10.1017/S0022112062000877.
- Munk, W., F. Snodgrass, and F. Gilbert (1964), Long waves on the continental shelf: An experiment to separate trapped and leaky modes, *J. Fluid Mech.*, *20*(4), 529–554, doi:10.1017/S0022112064001392.
- Munk, W. H. (1949), Surf beats, *AGU Trans.*, *30*(6), 849–854, doi:10.1029/TR030i006p00849.
- Okiihiro, M., and R. T. Guza (1996), Observations of Seiche forcing and amplification in three small harbors, *J. Waterw. Port Coastal Ocean Eng.*, *122*(5), 232–238, doi:10.1061/(ASCE)0733-950X(1996)122:5(232).
- Rawat, A., F. Arduin, V. Ballu, W. Crawford, C. Corela, and J. Aucan (2014), Infragravity waves across the oceans, *Geophys. Res. Lett.*, *41*, 7957–7963, doi:10.1002/2014GL061604.
- Rawlinson, N., and M. Sambridge (2004), Wave front evolution in strongly heterogeneous layered media using the fast marching method, *Geophys. J. Int.*, *156*(3), 631–647, doi:10.1111/j.1365-246X.2004.02153.x.
- Reniers, A. J. H. M. (2004), Morphodynamic modeling of an embayed beach under wave group forcing, *J. Geophys. Res.*, *109*, C01030, doi:10.1029/2002JC001586.
- Rhie, J., and B. Romanowicz (2006), A study of the relation between ocean storms and the Earth's hum, *Geochem. Geophys. Geosyst.*, *7*, Q10004, doi:10.1029/2006GC001274.
- Sheremet, A. (2002), Observations of nearshore infragravity waves: Seaward and shoreward propagating components, *J. Geophys. Res.*, *107*(C8), 3095, doi:10.1029/2001JC000970.
- Snieder, R. (2004), Extracting the Green's function from the correlation of coda waves: A derivation based on stationary phase, *Phys. Rev. E*, *69*(4), 046610, doi:10.1103/PhysRevE.69.046610.
- Symonds, G., D. A. Huntley, and A. J. Bowen (1982), Two-dimensional surf beat: Long wave generation by a time-varying breakpoint, *J. Geophys. Res.*, *87*(C1), 492–498, doi:10.1029/JC087iC01p00492.
- Toomey, D., et al. (2014), A sea change in seismological studies of subduction zones, *Oceanography*, *27*(2), 138–150, doi:10.5670/oceanog.2014.49.
- Tucker, M. J. (1950), Surf beats: Sea waves of 1 to 5 min. period, *Proc. R. Soc. London, Ser. A*, *202*(1071), 565–573, doi:10.1098/rspa.1950.0120.
- Uchiyama, Y., and J. C. McWilliams (2008), Infragravity waves in the deep ocean: Generation, propagation, and seismic hum excitation, *J. Geophys. Res.*, *113*, C07029, doi:10.1029/2007JC004562.
- Wapenaar, K., and J. Thorbecke (2013), On the retrieval of the directional scattering matrix from directional noise, *SIAM J. Imaging Sci.*, *6*(1), 322–340.
- Webb, S. C., X. Zhang, and W. Crawford (1991), Infragravity waves in the deep ocean, *J. Geophys. Res.*, *96*(C2), 2723–2736, doi:10.1029/90JC02212.
- Widrow, B., P. E. Mantey, L. J. Griffiths, and B. B. Goode (1967), Adaptive antenna systems, *Proc. IEEE*, *55*, 2143–2159, doi:10.1109/PROC.1967.6092.